

Cloud Properties Inferred from 8–12- μ m Data

KATHLEEN I. STRABALA AND STEVEN A. ACKERMAN

Cooperative Institute for Meteorological Satellite Studies, University of Wisconsin—Madison, Madison, Wisconsin

W. PAUL MENZEL

NOAA/NESDIS, Advanced Satellite Products Project, Madison, Wisconsin

(Manuscript received 16 November 1992, in final form 17 June 1993)

ABSTRACT

A trispectral combination of observations at 8-, 11-, and 12- μ m bands is suggested for detecting cloud and cloud properties in the infrared. Atmospheric ice and water vapor absorption peak in opposite halves of the window region so that positive 8-minus-11- μ m brightness temperature differences indicate cloud, while near-zero or negative differences indicate clear regions. The absorption coefficient for water increases more between 11 and 12 μ m than between 8 and 11 μ m, while for ice, the reverse is true. Cloud phase is determined by a scatter diagram of 8-minus-11- μ m versus 11-minus-12- μ m brightness temperature differences; ice cloud shows a slope greater than 1 and water cloud less than 1.

The trispectral brightness temperature method was tested upon high-resolution interferometer data resulting in clear-cloud and cloud-phase delineation. Simulations using differing 8- μ m bandwidths revealed no significant degradation of cloud property detection. Thus, the 8- μ m bandwidth for future satellites can be selected based on the requirements of other applications, such as surface characterization studies. Application of the technique to current polar-orbiting High-Resolution Infrared Sounder (HIRS)–Advanced Very High Resolution Radiometer (AVHRR) datasets is constrained by the nonuniformity of the cloud scenes sensed within the large HIRS field of view.

Analysis of MAS (MODIS Airborne Simulator) high-spatial resolution (500 m) data with all three 8-, 11-, and 12- μ m bands revealed sharp delineation of differing cloud and background scenes, from which a simple automated threshold technique was developed. Cloud phase, clear-sky, and qualitative differences in cloud emissivity and cloud height were identified on a case study segment from 24 November 1991, consistent with the scene. More rigorous techniques would allow further cloud parameter clarification.

The opportunities for global cloud delineation with the Moderate-Resolution Imaging Spectrometer (MODIS) appear excellent. The spectral selection, the spatial resolution, and the global coverage are all well suited for significant advances.

1. Introduction

The earth's radiation budget and climate are dependent upon cloud radiative and geometric properties. Clouds are both efficient absorbers of outgoing long-wave radiation and reflectors of incoming solar radiation. Due to their vital role, correct cloud parameterization is crucial for improved accuracy of climate models and for meeting the goals of the Earth Observing System (EOS).

The window region (8–12 μ m) is an important part of the infrared spectrum since terrestrial radiation peaks here. Cloud-detection techniques in the infrared also have a distinct advantage over visible techniques by providing complete temporal coverage. Past infrared window cloud-detection algorithms have used single-

band measurements or bispectral split-window techniques (Booth 1973; Inoue 1987, 1989). The 8–12- μ m spectral region is also important in ice and water microphysics; changes in radiative properties from 8 to 11 μ m and 11 to 12 μ m allow carefully chosen bands to differentiate cloud characteristics. To date, no single operational satellite contains all three bands in these spectral ranges that would allow both cloud detection and cloud particle property delineation.

This paper further investigates the capabilities of the trispectral infrared technique proposed by Ackerman et al. (1990), utilizing very high spatial resolution data from MAS, designed to meet the specifications outlined in EOS. Section 2 describes the trispectral technique development, including sensitivity of spectral selection to cloud microphysical properties and atmospheric structure. The algorithm is tested upon aircraft and operational satellite data in section 3 with discussions on channel bandwidth and instrument FOV effects. The capabilities of a trispectral technique are demonstrated at the end of section 3 using observations from

Corresponding author address: K. I. Strabala, CIMSS, Space Science and Engineering Center, University of Wisconsin, 1225 West Dayton Street, Madison, WI 53706.

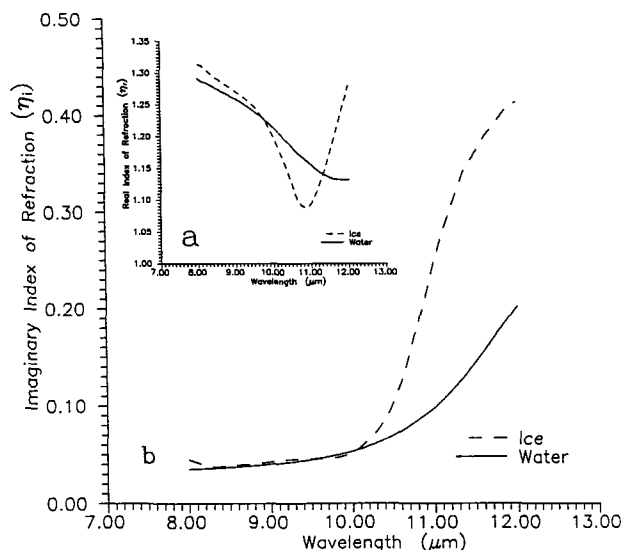


FIG. 1. Indices of refraction of ice and water across the atmospheric window: (a) real portion, (b) imaginary portion.

the MAS. These observations are also used to develop and test a cloud-retrieval algorithm. A comparison of the trispectral technique to a visible cloud detection method is made in section 4. Results are summarized in section 5.

2. Technique development

a. Physical principles

The radiative properties of clouds are defined by their single-scattering and geometric characteristics. The single-scattering properties are defined by the complex index of refraction, the cloud-particle size distribution, and the particle shape distribution. Remote sensing of clouds from a satellite platform must also consider the atmospheric absorption properties. This section discusses the underlying physical principles that determine the capabilities and channel bandwidths of the proposed trispectral technique.

Absorption and emission by clouds are dependent upon the index of refraction of the particle

$$m = n_r - n_i, \quad (1)$$

where n_r , the real portion, represents the magnitude of scattering by the particle, and n_i , the complex portion, is an indication of absorptive properties of the material. Figure 1 depicts the real and imaginary portion of the index of refraction (after Warren 1984) over the atmospheric window for both ice and liquid water. Differences in the values of the indices for water versus ice will result in distinctive reactions to similar incident radiation. An investigation of the bulk properties over the atmospheric window was undertaken to determine the optimum wavelengths for detecting ice versus water clouds.

Minimum values of the imaginary portion of the index of refraction occur from 8 to 10 μm (Fig. 1b), indicating weaker particle absorption. The ice and water indices increase and diverge beyond this spectral region. Based solely on the imaginary indices of refraction, more absorption will take place in ice clouds between 10 and 12 μm than in water clouds of equal water content. This results in lower blackbody temperatures for ice clouds than water clouds of similar height and thickness. Ackerman et al. (1990), noted that blackbody temperature decreases with increasing wavelength for thick cirrus between wavelengths of 10 and 12 μm. This is due to the increase in the absorption coefficient,

$$\kappa = \frac{4\pi n_i}{\lambda}, \quad (2)$$

whose shape closely resembles that of the imaginary index of refraction over this interval.

Cloud radiative processes are also dependent upon the size of particles in the cloud. A representative sample of particle sizes was chosen ranging from 5 (small water drops) to 30 μm (large ice spheres), to model the effects of particle size on the single-scattering properties. Mie theory applied to homogeneous spheres was used in this simulation.

Modeled results indicate single-scattering properties that closely match the general shape of the indices of refraction for the smaller particle sizes. For example, the single-scattering albedo (Fig. 2a), and the absorption efficiency (Fig. 2b), of 5- and 10-μm size particles mimic the shapes of the real and imaginary index of refraction of ice, respectively. Scattering processes are

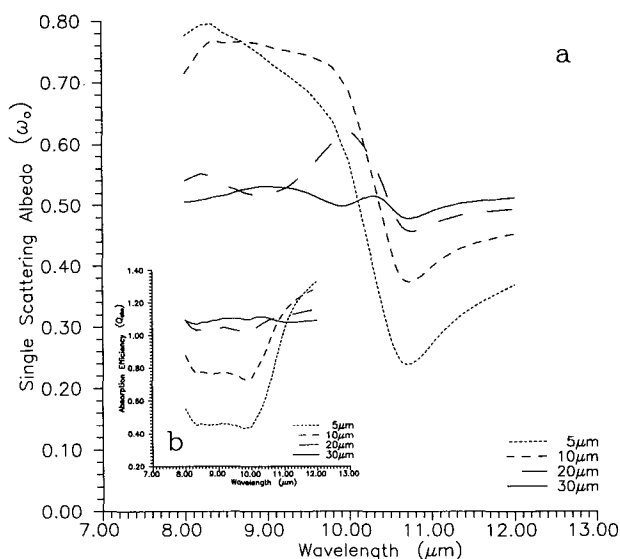


FIG. 2. (a) Single-scattering albedo of ice and (b) the absorption efficiency of ice, for four particle sizes (5, 10, 20, and 30 μm), across the 8–12-μm spectral region.

at a maximum in the 8–9- μm region and a minimum in the 10.5–12- μm region. Beyond this size range the spectral variation is reduced.

An investigation of cloud-particle shape revealed no significant differences in the spectral signature of the single-scattering properties between ice spheres and infinite cylinders. Scattering is greatest between 8 and 9 μm and at a minimum between 10.5 and 12 μm . Takano et al. (1992) showed similar results using spheroidal and hexagonal particles; scattering was greater at 8.3 μm than at 11 or 12 μm . Theoretical simulations using spheroidal and/or hexagonal particles agreed better with observed interferometer radiances, particularly at 8.3 μm , than assumed spherical particles.

The results of the single-scattering simulations indicate that:

- Scattering processes are greatest in the 8–9- μm region and at a minimum from 11 to 12 μm .
- Particle absorption is greatest from 11 to 12 μm and at a minimum from 8 to 10 μm .
- Single-scattering properties generally follow the pattern of the index of refraction until reaching a particle size of 30 μm .
- Spectral variations in single-scattering properties are largest in the 10–11- μm region.

To retrieve cloud properties, one must accurately account for the radiative properties of the atmosphere. Atmospheric energy transfer is dependent upon of the amount of absorption/emission, reflection, and transmission of energy in each layer. Scattering is negligible in the infrared region of the spectrum for clear sky, since the wavelengths are much greater than the size of air molecules. The total transmittances of a standard atmosphere were computed using Fast Atmospheric Signature CODE 2 (FASCOD2) for the 8–13- μm spectral region (Smith et al. 1991) and the resultant spectra is depicted in Fig. 3.

From 8 to 13 μm , the transmittance is generally greater than 0.7, meaning most of the energy emitted from the earth surface and atmosphere will escape to space (Fig. 3). An exception to this is the 9–10- μm region where transmittance values drop off to around 0.2 due to the ozone absorption band, centered at 9.6 μm . Much of the remaining spectral variations across the window are a result of water vapor absorption lines.

Combining the results of gaseous absorption with simulations of single-scattering properties, regions of the infrared spectrum can be selected that would be most useful for the detection of cloud.

In the 8–9- μm region, ice–water particle absorption is at a minimum, while water vapor absorption in the atmosphere is moderate. In the 11–12- μm region the opposite is true; particle absorption is at a maximum and atmospheric water vapor absorption is relatively small. Using bands in these two regions in tandem, cloud properties can be distinguished. As described in Ackerman et al. (1990), large positive brightness tem-

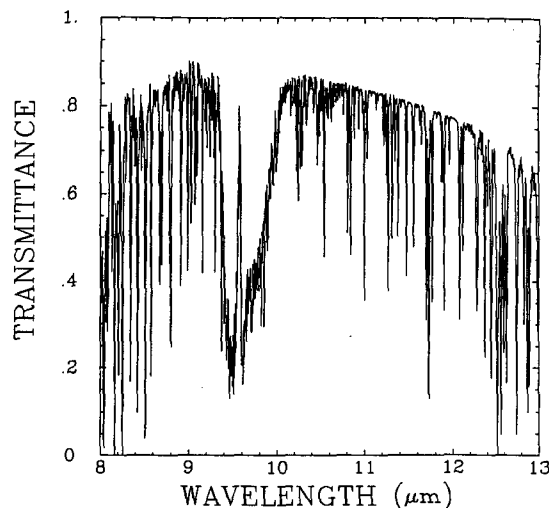


FIG. 3. HIS total transmittance spectra for a standard atmosphere across the 8–13- μm spectral region.

perature differences of 8 minus 11 μm indicate the presence of cirrus clouds. This is due to the larger increase from 8 to 11 μm in the imaginary index of refraction of ice over water (Fig. 1b). For clear conditions, the 8-minus-11- μm brightness temperature difference will be small or even negative due to stronger atmospheric water vapor absorption at 8 than 11 μm (Fig. 3). Therefore, clear conditions will be indicated by small or negative brightness temperature differences with cirrus cloud identified by large positive differences.

The 11- μm band is a spectral region of minimum scattering for both ice and water (Fig. 1a). Since the real part of the index of refraction of ice and water tends toward that of air, this is a region where particle scattering effects can be neglected.

Several 8- and 11- μm spectral band combinations can be chosen. One possibility has an 8- μm band chosen on a water vapor absorption line, and the 11- μm band chosen to exclude water vapor effects. This will ensure negative differences for clear conditions even in a tropical atmosphere where the slope of the transmittance as a function of wavelength is very steep over the 11- μm region. Other options include choosing bands that possess the same water vapor absorption effects so that differences can be related uniquely to cloud properties.

A narrowband between 10 and 10.80 μm is less useful due to the difficulty in modeling the large spectral changes that occur over this region by cloud particles. Also, the difference in the absorption coefficient of ice between 10–10.5 and 8 μm is too small to result in a positive brightness temperature difference, indicative of cirrus.

A third band in the 12- μm region will enable cloud phase delineation. Water-particle absorption increases more between 11 and 12 μm than between 8 and 11

μm , while the increase of ice-particle absorption is greater between 8 and 11 μm than between 11 and 12 μm (Fig. 1b). Thus the 11-minus-12- μm brightness temperature differences of water clouds are greater than the 8-minus-11- μm differences. Conversely, 8-minus-11- μm brightness temperature differences of an ice cloud scene are greater than coincident 11-minus-12- μm differences. Therefore, ice and water clouds will separate in a scatter diagram of 8-minus-11- μm versus 11-minus-12- μm brightness temperature differences, with ice clouds having a steeper slope than water clouds. Mixed-phase or partial-radiometer-filled ice over water clouds will exhibit characteristics of both ice and water clouds in this format, grouping in between the ice and water slopes. The maximum difference between ice and water absorption occurs near 12 μm ; using a band near this interval will also maximize the signal of ice versus water cloud in the 11–12- μm brightness temperature difference. Finally, the 9–10- μm spectral region should be avoided due to the strong absorption and emission of energy by ozone (Fig. 3). Ozone resides in greatest quantity in the stratosphere and its concentration varies with synoptic conditions. The amount of energy received from cloud versus that due to ozone emission would be difficult to distinguish.

Using arguments from both atmospheric absorption and single-scattering cloud particle properties, it emerges that a combination of spectral bands centered at 8, 11, and 12 μm appears to be the most useful combination of window region bandwidths for the purpose of cloud detection.

b. Trispectral technique

The essence of the trispectral method consists of interpreting a scatter diagram of 8-minus 11- μm versus 11-minus 12- μm brightness temperature differences. The clear region is expected to be represented by near-zero or negative values of 8-minus 11- μm and small 11-minus 12- μm differences. The magnitude of these differences will depend upon the total column water vapor amount. Water and ice cloud should separate in distinct clusters with ice clouds grouped along a slope greater than 1 and water cloud less than 1. Mixed-phase cloud, or mixed cloud scenes, will be identified by values in between (near the slope of unity). Ice and water clouds with emissivities less than 1 can be discerned by the large positive values they exhibit; large 8-minus 11- μm differences for ice cloud and large 11-minus 12- μm differences for water cloud. High-emissivity clouds are expected to exhibit near-zero values for both brightness temperature differences; however, ancillary information acquired from the three channels (11- μm brightness temperature and 8- μm radiance standard deviation) is expected to aid in the interpretation.

These anticipated results discussed above are for ideal clouds. Clouds are certainly not homogeneous in

the horizontal or vertical directions. Ice clouds are also much different than liquid water clouds. The water content of ice clouds is extremely variable (10^{-4} – 10^0 g m^{-3}), while water clouds have smaller variations (10^{-1} – 5.0×10^0 g m^{-3}). We can also expect water clouds to reside lower in the atmosphere where the temperature is warmer, which will aid in cloud classification. For example, a cloud with an equivalent blackbody temperature of 210 K can only be an optically thick ice cloud. However, a thin cirrus cloud can have the same equivalent blackbody temperature as a low-level water cloud, and it is this situation that the trispectral technique should help delineate. Water vapor is also vertically distributed, decreasing exponentially with altitude and will impact the detection of low-level clouds, as they will have more water vapor in the vertical column above cloud top than a high ice cloud. As water vapor distribution is highly variable in space and time, effective particle size may be better estimated for high ice clouds than for low-level water clouds. The variability of atmospheric water vapor also makes it difficult to select a single threshold or slope to distinguish water clouds from ice clouds. The variability of the water vapor in the atmosphere also has an impact on the clear-sky threshold. Our present approach is to base the clear-sky threshold on the trispectral difference, the magnitude of the 11- μm equivalent blackbody temperature, and a measure of the spatial variability. Over water, it would be extremely valuable to combine this method with visible observations to help select the clear-sky threshold. Finally, in our present discussions, we have assumed the emissivity at the surface to be the same at all three wavelengths. This is certainly not the case for bare soils, and adjustments will need to be made over desert surfaces. The next section explores the trispectral technique using measurements made from aircraft and satellite.

3. Results with aircraft and satellite data

The trispectral combination of 8-, 11-, and 12- μm bands appears to offer opportunities for delineating cloud properties. In this section, the technique is demonstrated with aircraft and satellite data and an investigation of appropriate bandwidths was undertaken.

a. Application to HIS observations and spectral sensitivity

During the First ISCCP (International Satellite Cloud Climatology Project) Region Experiment (FIRE), the High Spectral Resolution Interferometer Sounder (HIS) gathered data while flying on the NASA ER2. HIS data (Smith et al. 1986) covers 3.1–17 μm and has a resolution of approximately 0.5 cm^{-1} from 600 to 1100 cm^{-1} (9.1–16.7 μm) and 1.0-cm^{-1} resolution from 1100 to 2700 cm^{-1} (3.7–9.1 μm). The nadir spatial resolution is 2 km at ground level from an altitude of approximately 20 km.

The trispectral combination of bands was determined from an HIS dataset collected on 2 November 1986. Reference spectral regions of 8.3–8.4, 11.06–11.25, and 11.93–12.06 μm were chosen as per Ackerman et al. (1990). This trio of bandwidths will insure negative 8-minus-11- μm brightness temperature differences for clear FOVs along with positive 11-minus-12- μm differences. Plots of the brightness temperature differences show two distinct clusters of points (Fig. 4a). Utilizing collocated lidar data, Ackerman et al. (1990), demonstrated that the cluster of points with a slope greater than 1 is ice cloud. This same study found that all cloud-free points are encompassed by an 8-minus-11- μm brightness temperature difference less than -0.4 K. This threshold will change depending on

the amount of water vapor present, and the proximity of the 8- μm band to a water vapor line. In this example, there are two distinct groups of points with an 8-minus-11- μm brightness temperature difference less than the threshold. This is due to two distinct clear regions with differing average 8-minus-11- μm brightness temperature values; one over land (-1.2 K) and one over water (-2.0 K). In this instance, a single clear 8-minus-11- μm brightness temperature threshold value encompasses some liquid low-cloud values also, but does not affect ice cloud versus clear-sky differentiation.

Small shifts in wavelength in the 8- μm spectral region will lead to a change in the threshold value, but not to a change in the accuracy of detecting cirrus. To illustrate this, brightness temperature difference plots were

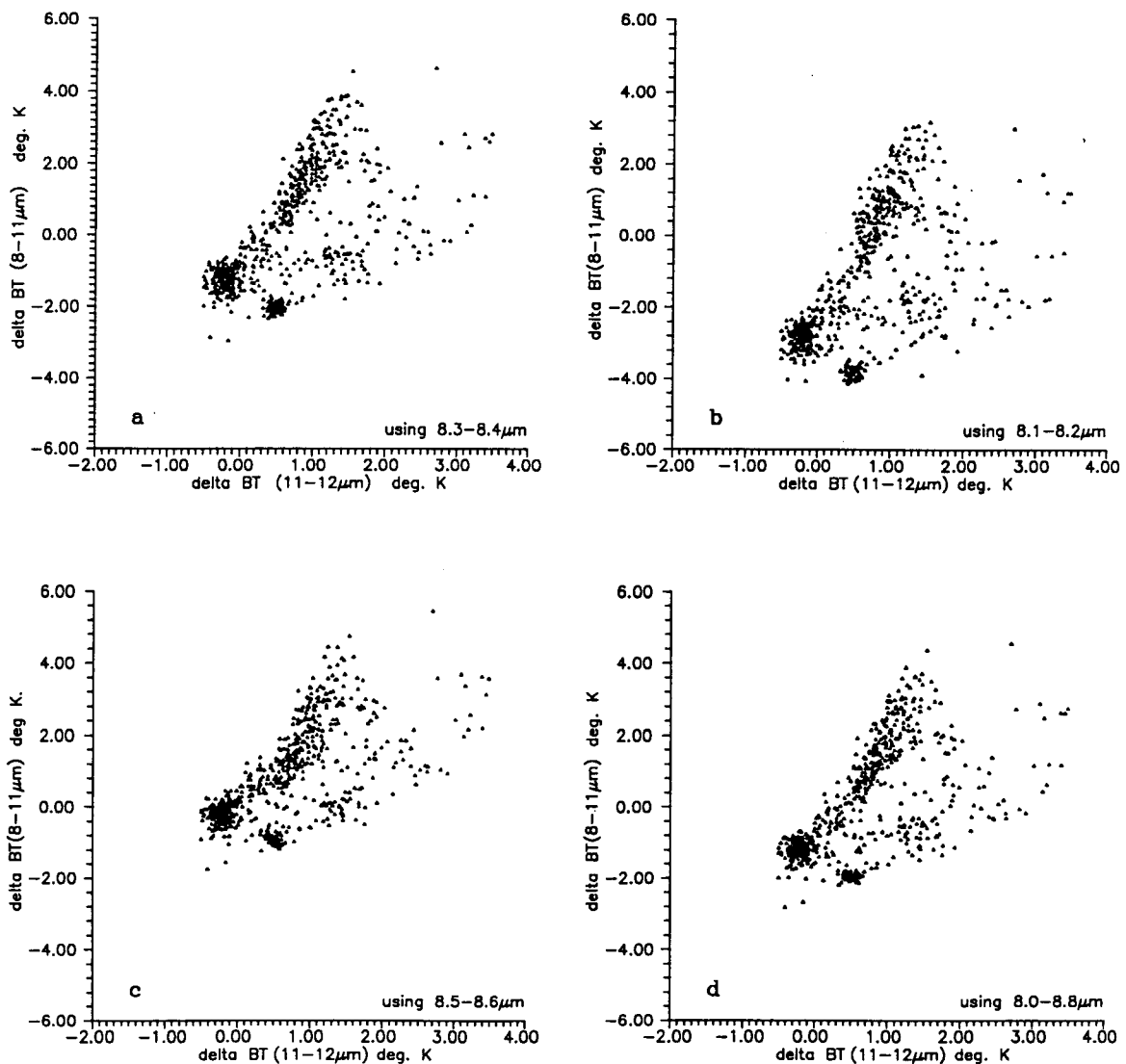


FIG. 4. Scatter diagrams of brightness temperature differences of 8–11 μm versus 11–12 μm for the HIS flight of 2 November 1986. Wavelength intervals 11.06–11.25 μm , 11.93–12.06 μm , and (a) 8.3–8.4 μm , (b) 8.1–8.2 μm , (c) 8.5–8.6 μm , and (d) 8.0–8.8 μm were used.

compared varying the location and width of the 8- μm band. As was previously noted, the 8.3–8.4- μm interval is located over a weak water vapor absorption band. If a stronger absorption interval is used, such as 8.1–8.2 μm (Fig. 3), the result is to shift the entire plot down (Fig. 4b), including the cloud-free threshold value. Conversely, choosing an off-line interval, such as 8.5–8.6 μm , leads to a general shift of data points toward positive values (Fig. 4c). This off-line position results in less scatter in the diagram due to the smaller influence of atmospheric water vapor. Notice in both plots that the two-cluster structure of the data is conserved, one with a slope greater than 1 and one with a slope less than 1; however, the threshold for cloud versus clear separation will be a function of channel bandpass and atmospheric structure.

A bandwidth more typical of an orbiting remote sensing instrument (8.0–8.8 μm) was also used in the brightness temperature difference comparisons. The spectral interval chosen, which is broad enough to encompass more than one water vapor absorption line, preserves the basic structure necessary to distinguish cloud properties (Fig. 4d).

b. Application to HIRS–AVHRR observations and FOV sensitivity

Trispectral brightness temperature differencing was applied to High-Resolution Infrared Sounder (HIRS-2) observations on *NOAA-9*, which contain an 8- μm (centered on 8.16 μm) and 11- μm band (centered on 11.2 μm) combined with Advanced Very High Resolution Radiometer (AVHRR) observations that provided the 11- μm (10.3–11.3 μm) and 12- μm (11.4–12.4 μm) bands. The collocation of the AVHRR observations within a given HIRS footprint was accomplished using the technique of Aoki (1980). The nadir FOV (field of view) for the HIRS is 17.4 km and the nominal FOV of AVHRR GAC (global area coverage) data is 4 km. All AVHRR pixels falling within an HIRS FOV were averaged into a single brightness temperature.

Figure 5 (top panel) is a plot of the HIRS 8-minus-11- μm versus the AVHRR 11-minus-12- μm data of a mixed-layer, multiphase cloud scene on 1 October 1986 over the Pacific Ocean. When compared to similar diagrams using HIS data, significant differences are noted. First, the 8-minus-11- μm brightness temperature cloud-free threshold is less defined and shifted downward. This is due to the high concentration of water vapor in the tropics. Secondly, the division evident in HIS data between ice and water clouds is not apparent. The diminished cloud property delineation seen in this satellite instrument dataset is due to the number of mixed-cloud scenes observed by the large HIRS footprint size. These nonuniform FOVs cause a blurring of the distinct cloud property structures apparent from the HIS data scatter diagrams. When the scatter dia-

gram includes only HIRS–AVHRR data over uniform cloud scenes (Fig. 5 lower panel) patterns emerge; the clear region (c), uniform water cloud (b), and uniform ice cloud (a) separate nicely. The division between the two phases is less defined, though the ice cloud lies above the line with unity slope. The areas of thin ice and water cloud, which clustered in such a coherent linear pattern in the HIS dataset, cannot be discerned here. Slopes of nonopaque pure ice or pure water cloud cannot be separated. Only the opaque classifications remain with the help of ancillary information. The HIRS–AVHRR combined dataset can, therefore, provide information on cloud properties from the trispectral method using proper uniformity screening. This also implies that brightness temperature differencing can be applied to smaller datasets over specified ground and/or cloud scenes, yielding useful results (Ackerman et al. 1992). High-resolution datasets, such as the HIS 2-km observations, are more likely to view uniform scenes, allowing the trispectral technique to be directly applied, as shown in section 3a.

c. Application to MAS observations and automated trispectral technique

The trispectral brightness temperature differencing has been tested with high-resolution interferometer and more coarse resolution operational polar-orbiting filter radiometers. Results suggest that the 8-, 11-, and 12- μm bands will serve the MODIS instrument as a means of determining cloud properties (King et al. 1992). The MAS was developed and tested as a prototype to the MODIS. The MAS instrument is a 50-channel spectrometer, flown on the NASA ER2 with a ground-level nadir FOV of 50 m, that collects data in the visible, shortwave infrared, midinfrared, and thermal spectral regions. Table 1 summarizes the MAS spectral characteristics as configured for the 1991 FIRE experiment.

For this study, the FIRE flight of 5 December 1991 was chosen due to the variety of scenes present. Figure 6 outlines the ER2 flight tracks discussed in this section overlaid on the 1500 (Fig. 6a) and 1900 UTC (Fig. 6b) GOES (Geostationary Operational Environmental Satellite) visible images.

MAS images of an optically thin cirrus cloud over Oklahoma (track A) from the three infrared spectral bands and the visible channel are shown in Fig. 7. Emissivity values less than 1 are evident by the lack of visible reflectivity of the cloud and by land features (e.g., river outline) that can be observed through the entire width of the cloud in the thermal data. The 11- μm brightness temperature values are generally less than 275 K, and collocated lidar data estimates cloud height to be 12 km, so the cloud is assumed to be composed of ice crystals.

A scatterplot of MAS brightness temperature differencing is in agreement with previous results from the HIS observations (Fig. 8, black dots). Single

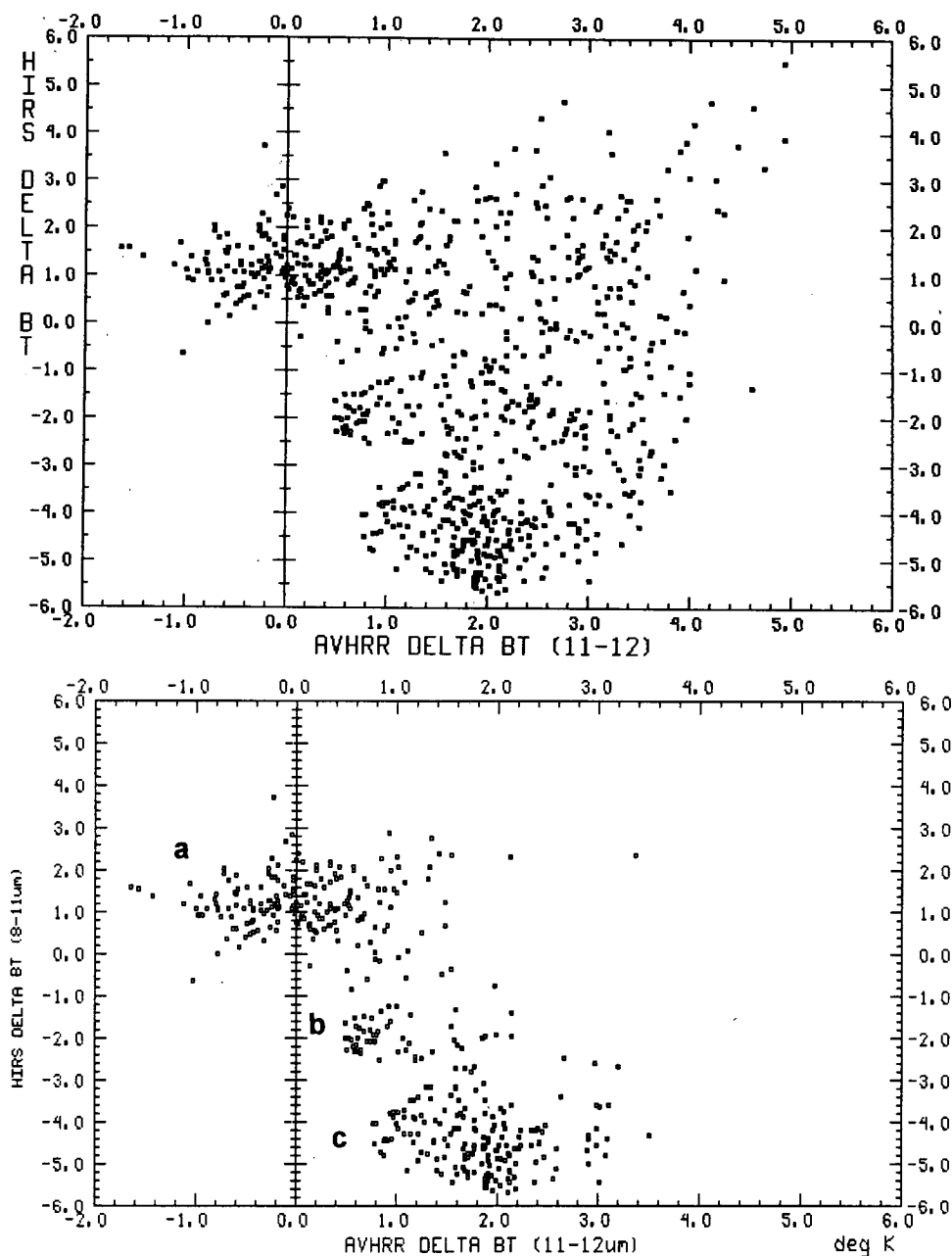


FIG. 5. Scatter diagram of brightness temperature differences from collocated HIRS 8-11- μm versus AVHRR 11-12- μm data collected on 1 October 1986. Complete dataset (upper panel), and dataset including only scenes where the standard deviation of the AVHRR 11- μm brightness temperature is less than 4.0 K (lower panel). The clusters of points represent (a) uniform ice cloud, (b) uniform water cloud, and (c) clear-sky scenes.

sample noise necessitated averaging to at least 250-m resolution (25 FOVs). In the examples shown in this paper, averaging was increased to 100 FOVs, reducing the resolution to 500 m. This resolution is still much greater than that observed from current operational satellites. A 30-pixel \times 46-pixel area was chosen over the center of the scene, amounting to 1380 data points used in the scatter diagrams. All

MAS scatter diagrams contain the same number of data points. Local zenith angle effects were minimized by limiting the area to $\pm 17^\circ$ from nadir. The cirrus cloud shown in Fig. 7 stands out as a cluster of points in a line with a slope greater than one, and a maximum 8-minus-11- μm brightness temperature difference value of 4 K. The coherent pattern suggests that thin cirrus is detected.

TABLE 1. MAS infrared spectral characteristics as configured for FIRE.

Data channel	Channel frequency (μm)	Half-power bandwidth (μm)
2	0.68	0.01
3	1.64	0.05
4	1.98	0.05
5	2.13	0.05
6	2.18	0.05
7	3.75	0.15
8	4.50	0.15
9	4.65	0.15
10	8.80	0.40
11	10.95	0.50
12	11.95	0.50

Another example, collected earlier in the flight, involves a low stratocumulus water cloud located over the Gulf of Mexico (track D). The $11\text{-}\mu\text{m}$ brightness temperatures in this scene range between 270 and 295 K. The brightness temperature difference scatter diagram for this water cloud is a group of points aligned in a slope less than 1 (Fig. 8, gray dots). Displaying the two cloud types on the same scatter diagram clearly shows the separation between ice cloud and water cloud.

A thick convective cirrus cloud over the gulf was also investigated (track E). These data were divided into 15-K intervals of $11\text{-}\mu\text{m}$ brightness temperature,

to identify the location of the scatter points in the image (Fig. 9). A coherent pattern is evident. The warmest brightness temperatures (290–305 K) are clustered in a circular pattern, coincident with the minimum 8-minus- $11\text{-}\mu\text{m}$ brightness temperature differences (0 to -1 K); this is the cloud-free region. As the cloud-top altitude increases and/or the optical thickness increases, the points continue in a pattern with a slope greater than 1, representative of ice cloud, peaking at an 8-minus- $11\text{-}\mu\text{m}$ brightness temperature value of 4 K. Continuing through colder brightness temperature values toward the center of the cloud, the emissivity values increase as the optical depth of the cloud increases, as evidenced by the very high reflectivity of the cloud in the visible. This causes the shape of the brightness temperature scatterplot to curve back toward zero. As Inoue (1987), noted, this represents a black cloud, where each of these infrared windows senses the cold cloud tops at the same temperature. This simple scatter diagram reveals clear regions, cloud phase, and qualitative differences in cloud height and cloud emissivity.

Thus far we have presented MAS results with single cloud types and single cloud layers. Example results for a multilayer, multiphase cloud situation are now discussed. Figure 10 is a two-panel (visible and $11\text{-}\mu\text{m}$ averaged) image of a multicloud scene over the Gulf of Mexico (track B). Cloud types range from thick ice cloud covering the left-central portion of the image, to low water cloud over the right side. Thin cirrus overlays

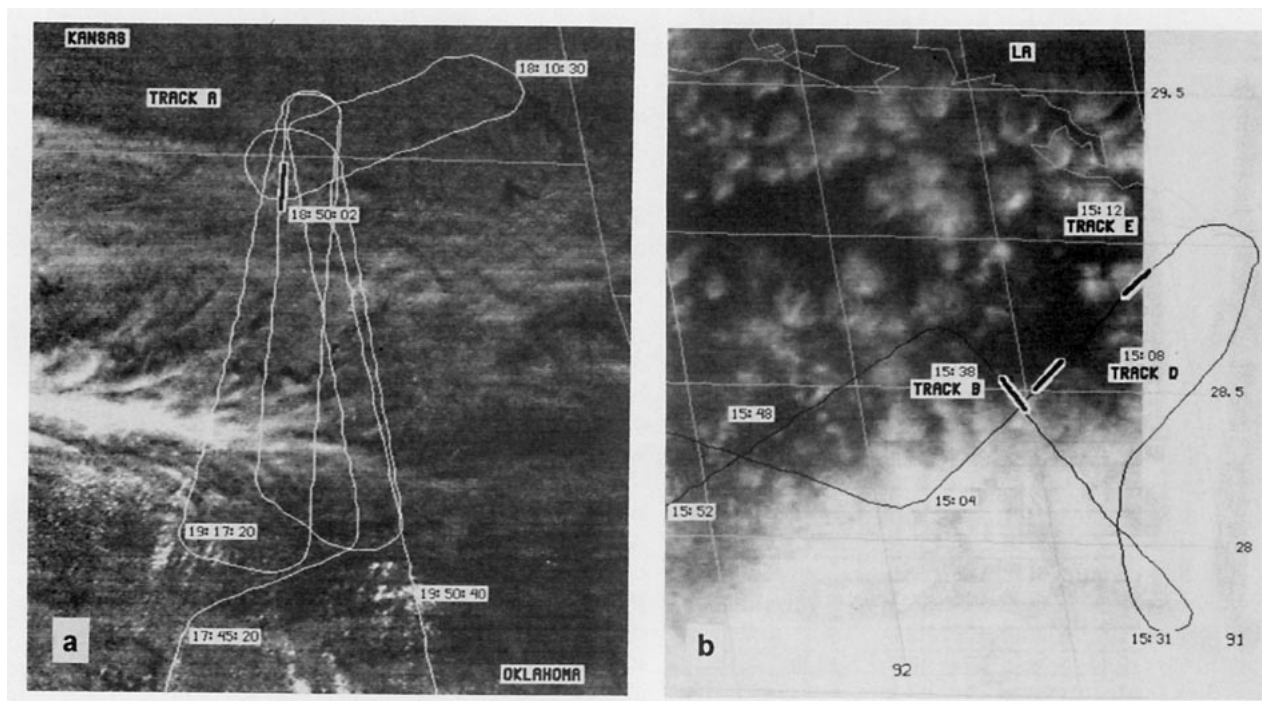


FIG. 6. NASA ER2 flight tracks overlaid on the GOES 1-km resolution visible images from the 5 December 1991 flight (a) over Oklahoma–Kansas at 1900 UTC and (b) over the Gulf of Mexico at 1500 UTC. Segments discussed in the text are outlined in bold.

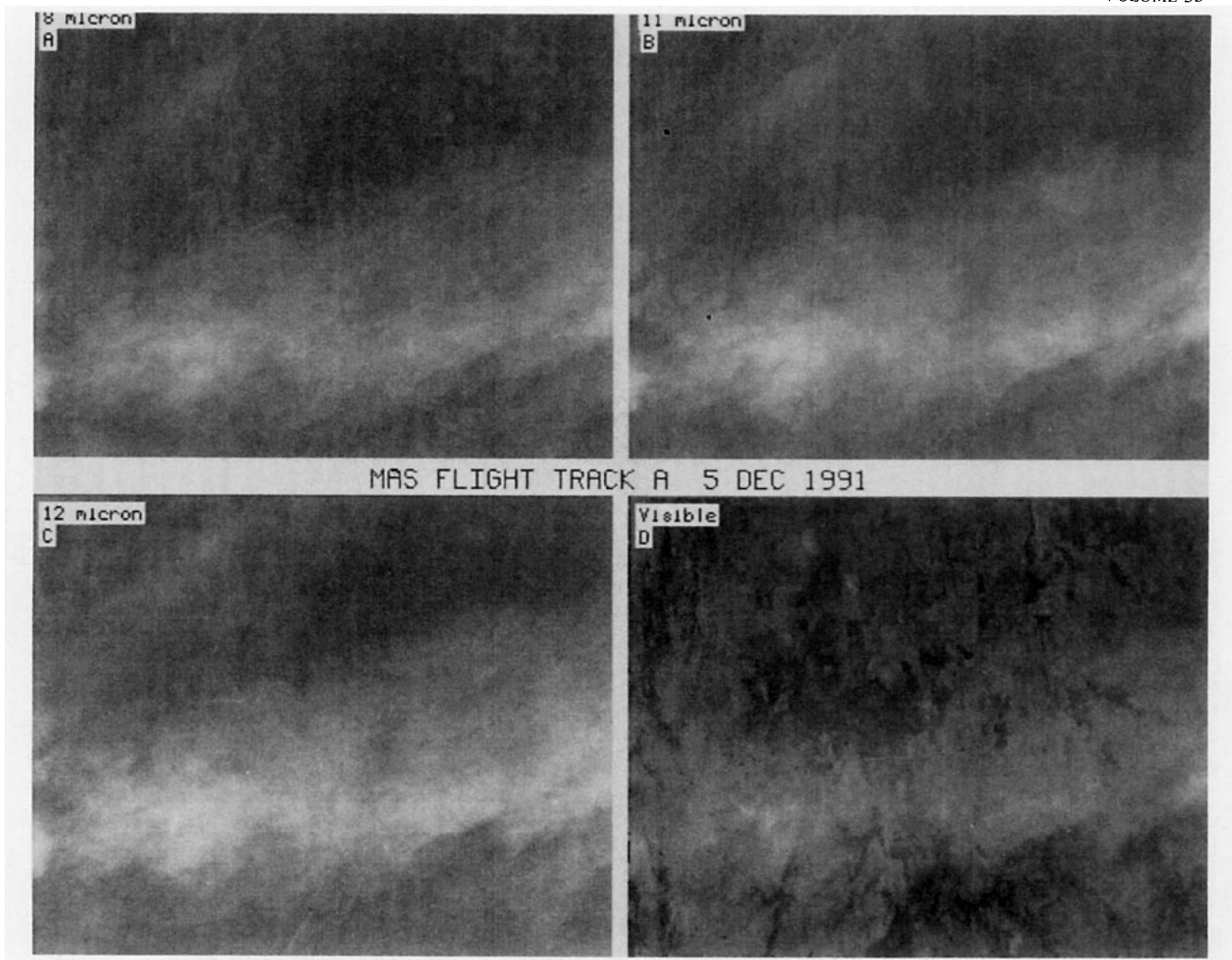


FIG. 7. MAS 50-m resolution: (a) 8 μm , (b) 11 μm , (c) 12 μm ; and (d) visible images of a thin ice cloud (track A) at 1850 UTC December 1991. Note the river outline that is apparent through the cloud.

the water cloud in the top center portion and a clear region dominates the lower image. The boxes represent differing cloud regimes observed in the visible image.

The scatter diagram of brightness temperature differences for the whole scene is less coherent than in previous examples (Fig. 11); however, features are still apparent. This becomes more evident when brightness temperature differences of the subscenes from Fig. 10 are plotted separately on a scatter diagram (Fig. 12). The clear region is still defined as a clustering of points with low 8-minus-11- μm brightness temperature differences (Fig. 12, scene 1). In this case, the 11-minus-12- μm difference for the clear region is between 1 and 2 K. Thin cirrus is defined by the line connecting the clear region with the largest 8-minus-11- μm brightness temperature differences, in this case 4 K (Fig. 12, scene 2). Thick cirrus is evident by the group of points that tend back toward the origin from peak 8-minus-11- μm differences (Fig. 12, scene 3). Water cloud can be

identified by the group of points aligned with a slope of less than 1 extending from opaque water (Fig. 12, scene 4) to lower-emissivity water cloud with the largest 11-minus-12- μm brightness temperature differences, in this case 4 K (Fig. 12, scene 5). Less easy to define are the points that lie close to the slope of unity, or in between the ice-water cluster of points (Fig. 12, scene 6). These points are representative of ice cloud over water cloud and, as such, exhibit characteristics of both.

It is important to compare the multicloud MAS brightness temperature scatter diagram with the HIRS-AVHRR results from a similar (but not the same) cloud scene discussed in section 3b (Fig. 5 upper panel). The MAS scatter diagram exhibits a distinct clear region (cluster of points near zero 8-minus-11- μm brightness temperature difference, and 11-minus-12- μm difference of 1–2 K), water clouds with high emissivities (points near zero 8-minus-11- μm brightness temperature difference and 11-minus-12- μm dif-

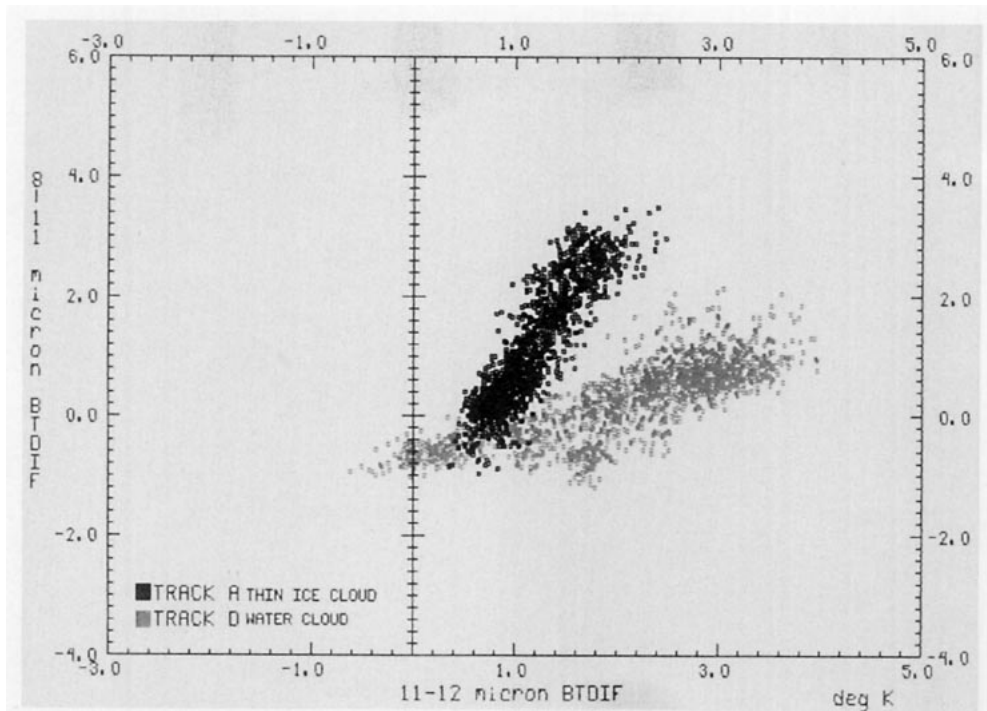


FIG. 8. Scatter diagram of averaged brightness temperature differences 8–11 μm versus 11–12 μm of the thin ice cloud (black dots) shown in Fig. 7 taken from the 1850 UTC MAS flight track dataset (track A), and of a water cloud (gray dots) taken from the 5 December 1991 1508 UTC MAS flight track dataset (track D).

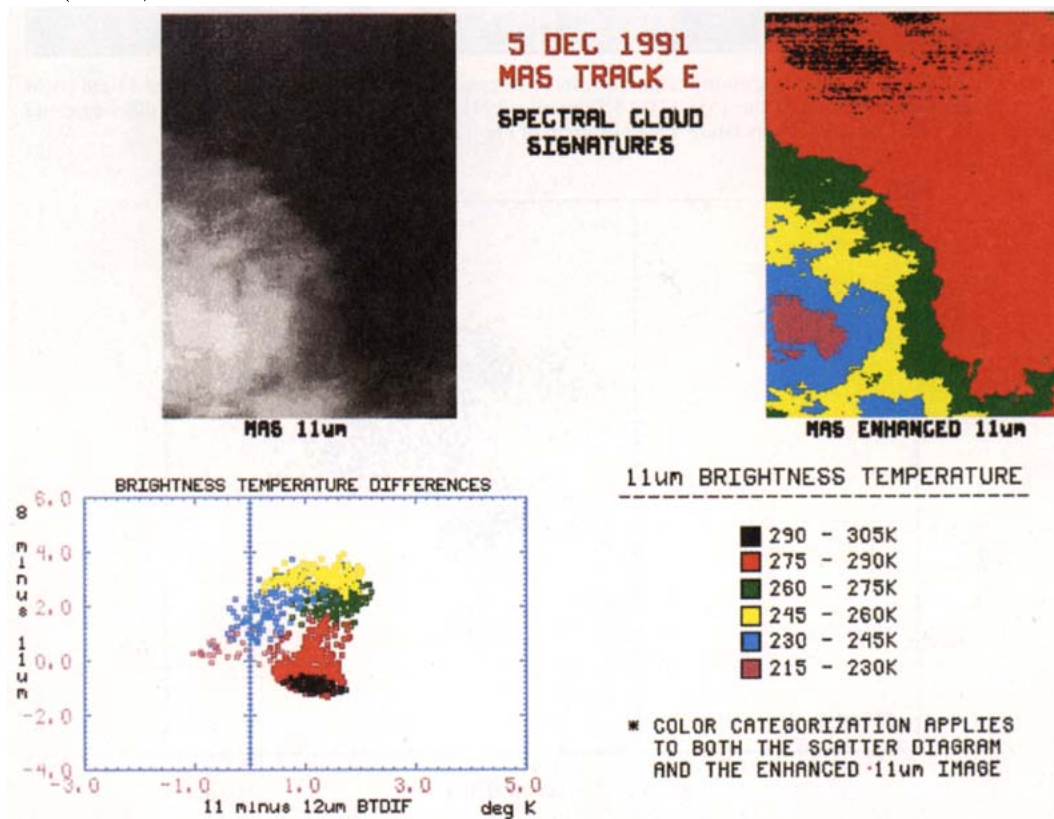


FIG. 9. MAS 50-m resolution 11- μm brightness temperature image of a thick ice cloud taken from 1512 UTC 5 December 1991 (track E) with no enhancement (upper left), and categorized in terms of brightness temperature (upper right). The brightness temperature difference scatter diagram (lower left) is coincidentally categorized.

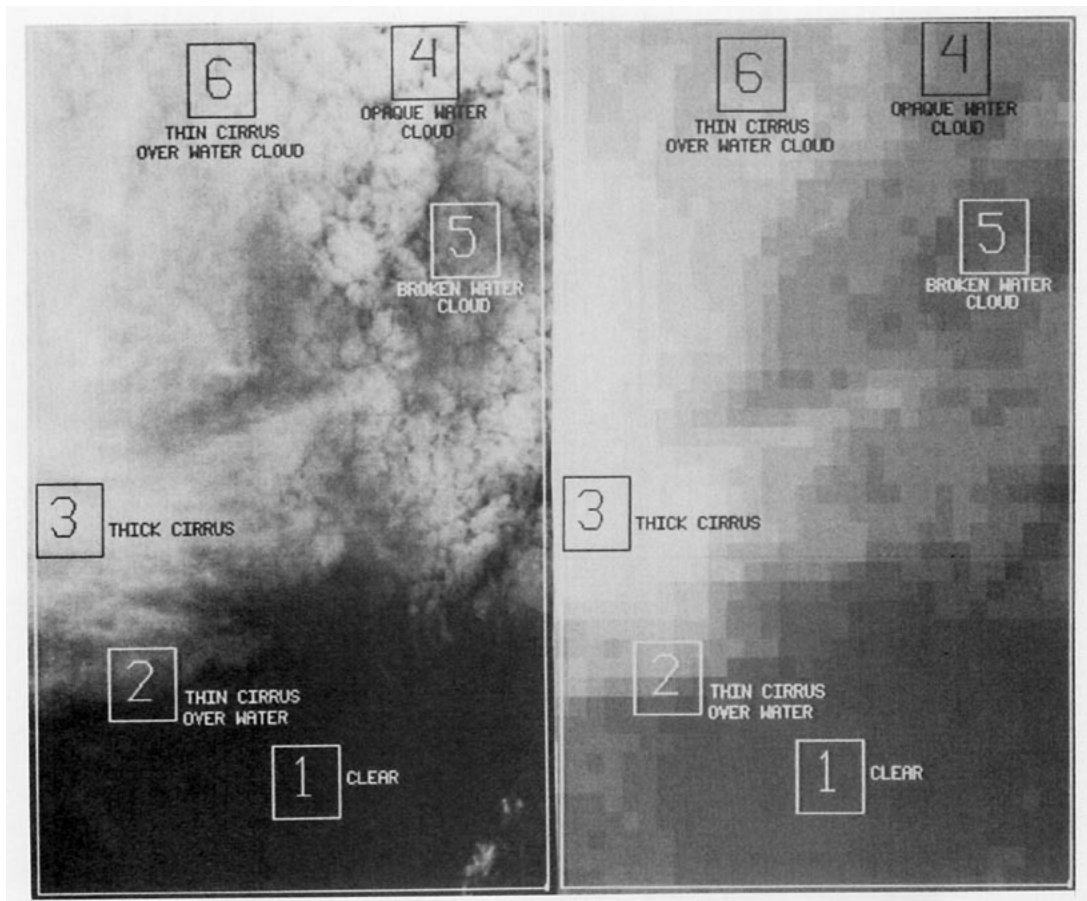


FIG. 10. MAS mixed-cloud scene 50-m resolution visible (left panel) and 10-pixel \times 10-pixel averaged 11- μ m (right panel) images from a portion of the 1538 UTC 5 December 1991 data (track B). Boxes represent differing cloud regimes used in the brightness temperature scatter diagram of Fig. 12.

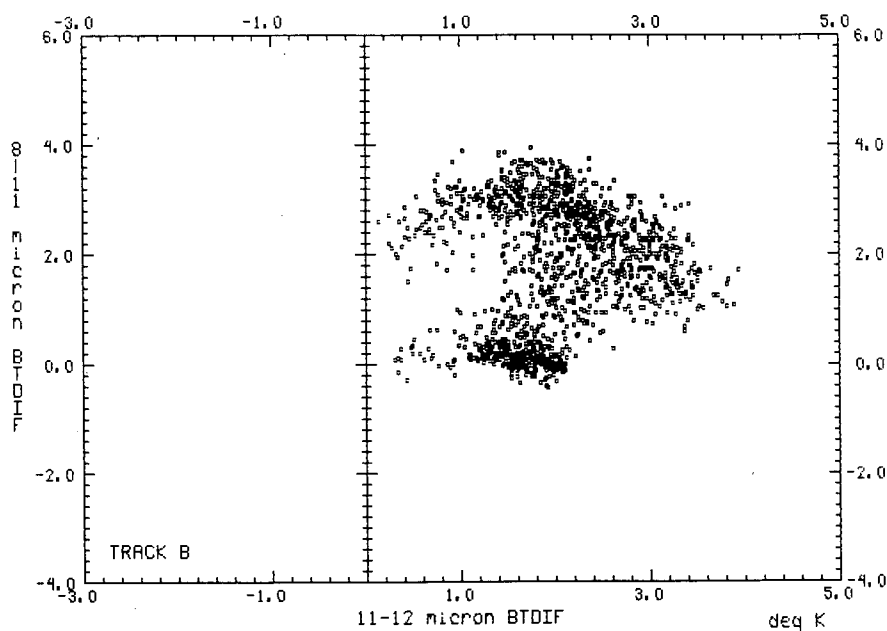


FIG. 11. Scatter diagram of averaged brightness temperature differences 8-11 μ m versus 11-12 μ m of the multiphase cloud scene of Fig. 10 taken from the 1538 UTC 5 December 1991 MAS flight track dataset (track B).

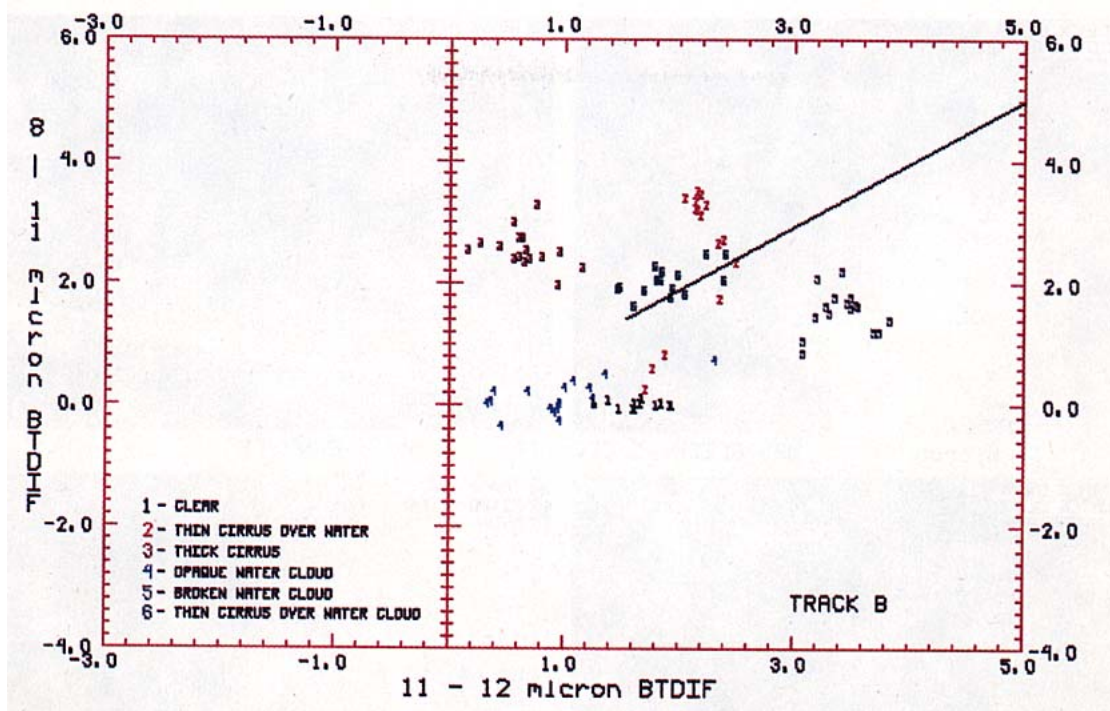


FIG. 12. Same as Figure 11 except limited to the cloud scenes identified in Fig. 10. Also shown for reference is a line with a slope of 1.

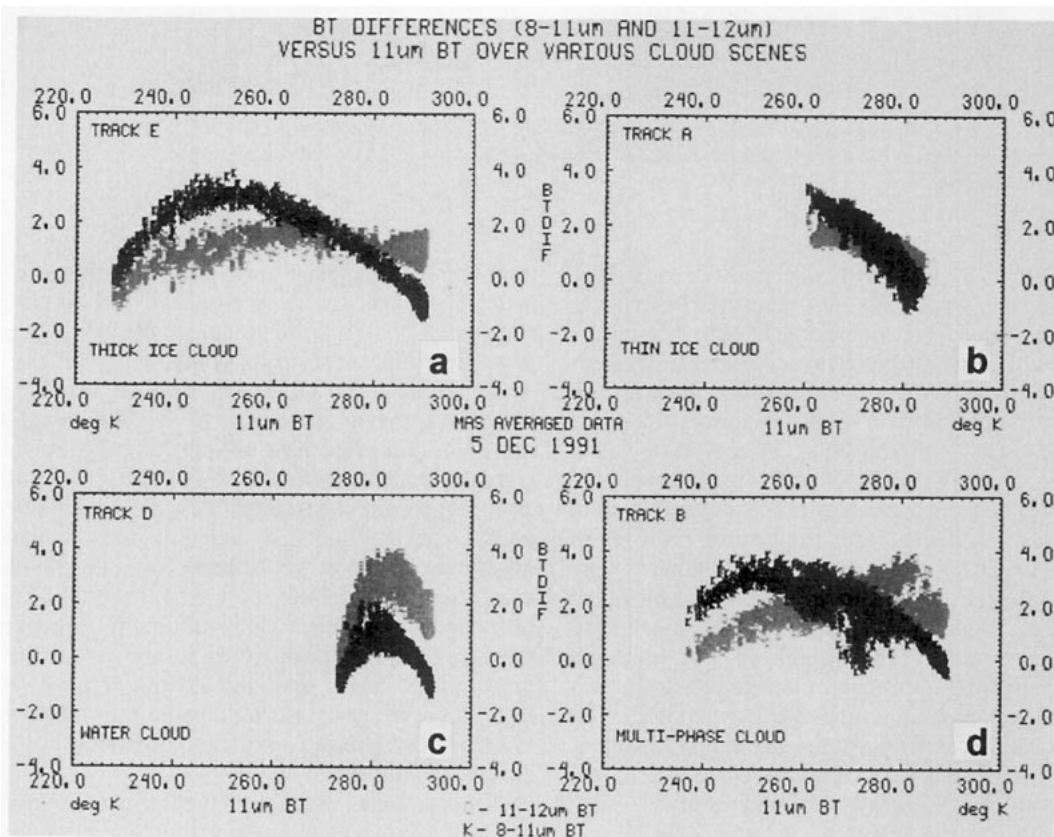


FIG. 13. MAS scatter diagram of 8-11- μm (black) and 11-12- μm (gray) brightness temperature differences versus the 11- μm brightness temperature for varying cloud scenes: (a) thick ice cloud, (b) thin ice cloud, (c) water cloud, and (d) multilayer, multiphase cloud. Note how the signature patterns of (a), (b), and (c) can also be observed in (d).

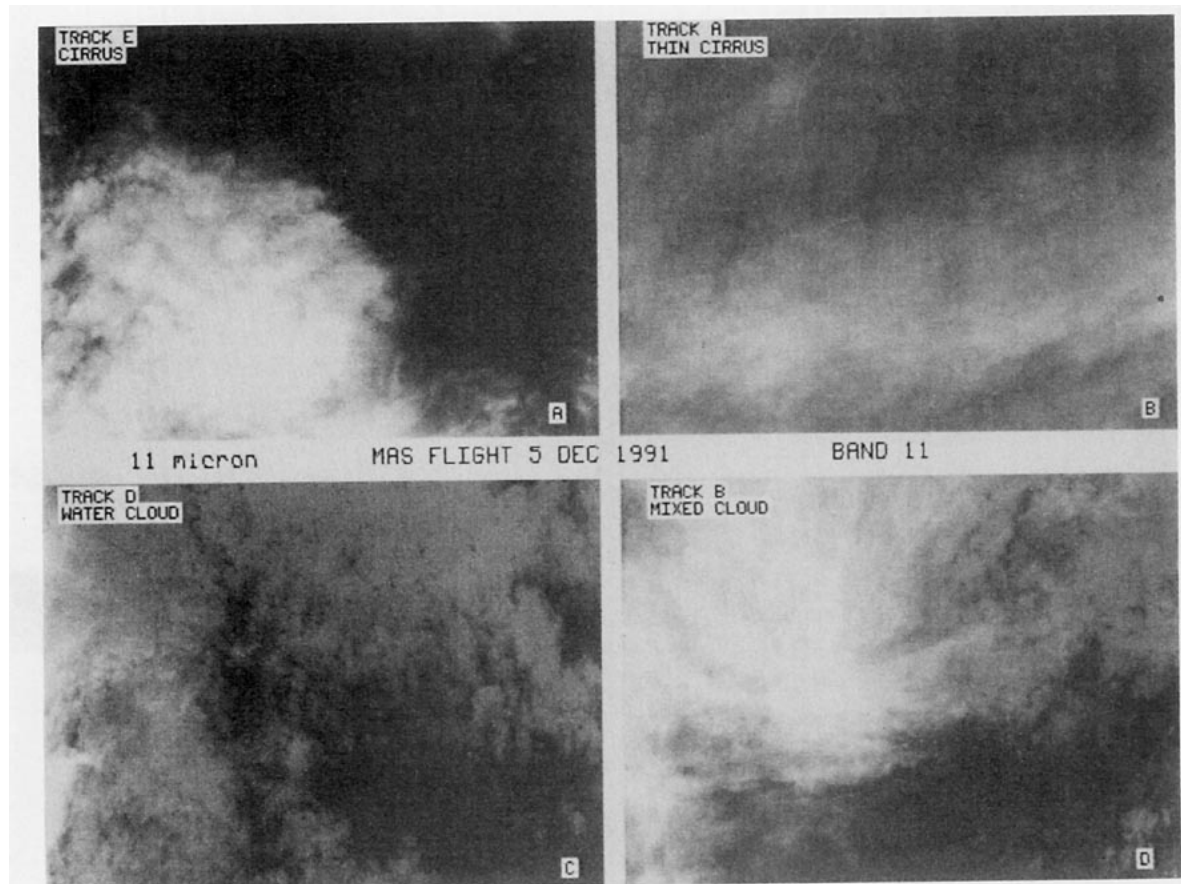


FIG. 14. MAS 50-m resolution images taken of varying cloud scenes from the 5 December 1991 ER2 flight. The scenes of (a) thick ice cloud, (b) thin ice cloud, (c) water cloud, and (d) multiphase cloud correspond to the scatter diagrams of Fig. 13.

ferences less than 1), ice clouds with higher emissivities (8-minus-11- μm brightness temperature differences greater than 1.5 K and 11-minus-12- μm differences less than 1 K), lower emissivity ice cloud and water cloud (maximum 8-minus-11- μm differences for ice and maximum 11-minus-12- μm differences for water cloud), and inferred mixed-layer/mixed-phase cloud in between. Almost none of these features can be distinguished using the unscreened HIRS-AVHRR data.

As a means of further differentiating multiphase cloud, the brightness temperature differences were plotted versus the 11- μm brightness temperature, as undescribed by Inoue (1987) (Fig. 13). All four cloud situations discussed so far are presented (Fig. 14), with black the 8-minus-11- μm brightness temperature differences and grey the 11-minus-12- μm differences. The top two panels, tracks E and A, are the ice cloud scenes. Track E is the black cloud case where the differences eventually go to 0 (zero) with decreasing 11- μm brightness temperatures. Again, the range of 8-minus-11- μm brightness temperature differences are greater than the 11-minus-12- μm difference range for both these examples. Track A is the thin cirrus scene. Note

that the 11- μm brightness temperatures are much higher in this scene than for track E and that the lower emissivity of the cloud prevents the brightness temperature differences from going to zero. The water cloud scene, track D, covers a much smaller 11- μm brightness temperature domain. In this case, the 11-minus-12- μm brightness temperature difference range is greater than the 8-minus-11- μm difference range. The arch formed in the scatter diagram again shows the points peaking and then curving back toward zero brightness temperature differences, as the 11- μm temperature decreases. Inoue (1987), described this phenomenon as low-level black clouds, physically due to the fact that the majority of water vapor lies below these clouds. As the scattered to broken low-level cloud layer becomes overcast, less water vapor below cloud level can be detected and the brightness temperature differences approach 0.

The final panel, track B, is the multilayer cloud scene where the patterns from the other three panels are all evident; in addition, thin cirrus cloud over low water cloud can be discerned from the arch of points from the low overcast black water cloud (around 270 K)

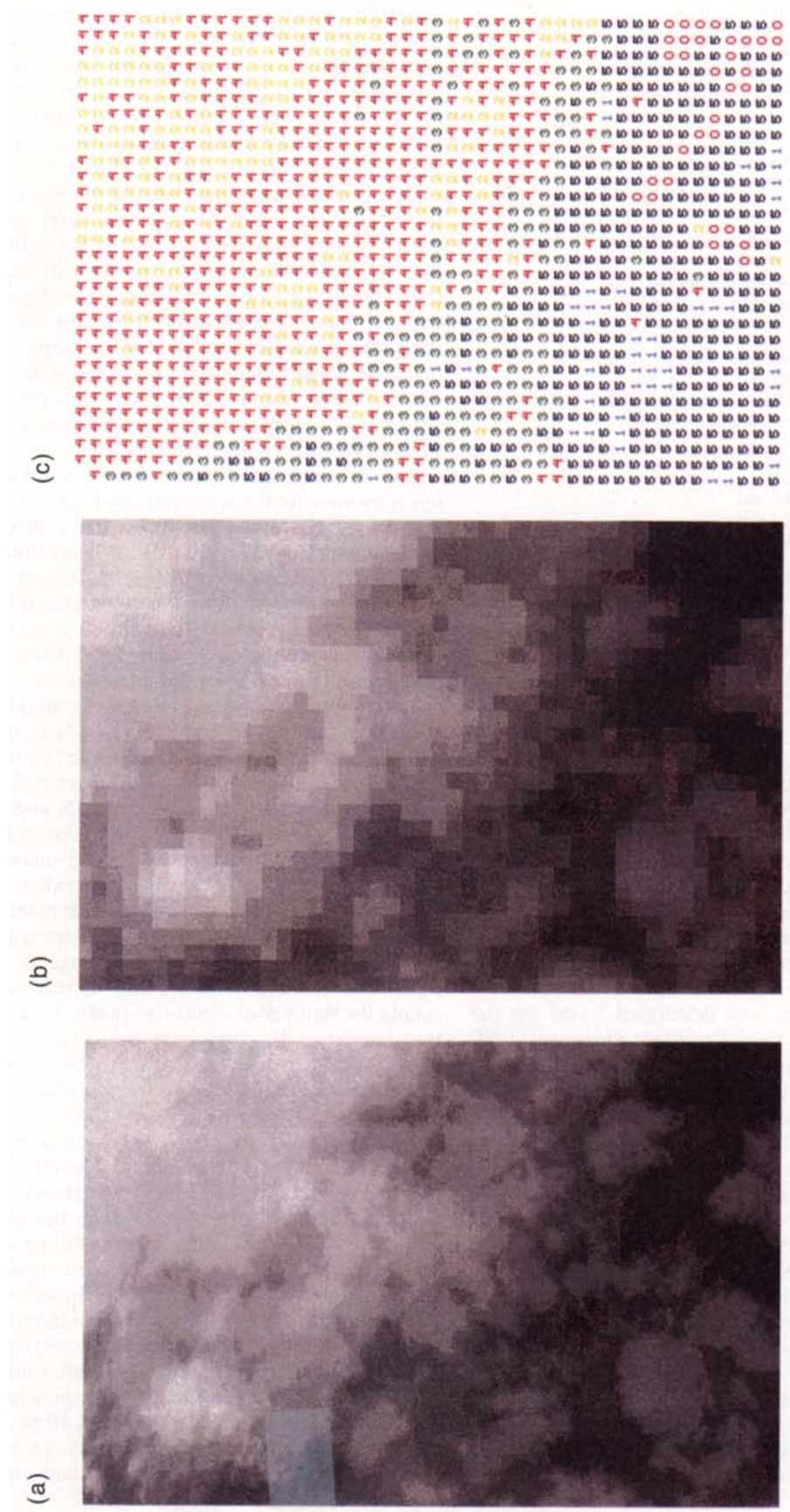


FIG. 15. MAS (a) 50-m and (b) 500-m resolution 11- μ m images of data taken from the 24 November 1991 ER2 flight and (c) the resultant trispectral algorithm diagram of coded cloud parameters coincident with each FOV in the 500-m resolution data.

TABLE 2. Thresholds of the trispectral technique applied to 10-pixel \times 10-pixel areas, where SD is the standard deviation, BT is the brightness temperature, BTDIF is the brightness temperature difference, and ABS is the absolute value.

Clear over water (code 0)	
if 8- μ m radiance SD < 0.5 and	
if 8-11- μ m BTDIF < 0.5 and	
if 11-12- μ m BTDIF < 2.4 and	
if 11- μ m BT > 277 K	
Water cloud with emissivity near one (code 1)	
if 8- μ m radiance SD < 0.5 and	
if clear 8-11- μ m BTDIF threshold not met and	
if 11-12- μ m BTDIF threshold not met and	
if 260 K < 11- μ m BT < 277 K	
Ice cloud with emissivity near one (code 2)	
if 8- μ m radiance SD < 0.5 and	
if clear 8-11- μ m BTDIF threshold not met and	
if 11-12- μ m BTDIF threshold not met and	
if 11- μ m BT < 260 K	
Mixed phase cloud (code 3)	
if 8- μ m radiance SD > 0.5 and	
if 8-11- μ m BTDIF > 1.25 and	
if the ABS of 8-11- μ m BTDIF minus 11-12- μ m BTDIF < 0.3	
Ice cloud with emissivity less than 1 (code 4)	
if 8- μ m radiance SD > 0.5 and	
if 8-11- μ m BTDIF minus 11-12- μ m BTDIF > 0.3	
Water cloud with emissivity less than 1 (code 5)	
if 8- μ m radiance SD > 0.50 and	
if 8-11- μ m BTDIF minus 11-12- μ m BTDIF < 0.3	

extending into the cirrus arch, combining with it around 255 K. The shape of the curves is very similar to that of the theoretical curves calculated by Inoue (1987), of the cirrus underlaid by low-level black clouds. Use of this scatter diagram then, in tandem with the 8-minus-11- μ m versus the 11-minus-12- μ m brightness temperature difference scatter diagram have the potential to differentiate multilayer and multiphase clouds.

A simple algorithm was developed based on the scatter diagrams from the differing cloud scenes, to differentiate thick ice and water cloud (emissivities near 1), ice and water cloud with emissivities less than 1, and mixed-phase cloud. The technique itself consists of a series of thresholds using both the 8-minus-11- μ m and 11-minus-12- μ m brightness temperature differences, the 11- μ m brightness temperature, and the 8- μ m radiance standard deviation. The test was performed on 10 \times 10 averaged pixel data (500-m resolution) from the 24 November 1991 ER2 FIRE flight over the Gulf of Mexico.

A complicated cloud scene was chosen for the test, consisting of multilayer, multiphase cloud with scattered clear patches (Figs. 15a,b). Each 10 \times 10 pixel was coded according to the technique outlined in Table 2. Clear and opaque (thick) cloud are distinguished from mixed and thin cloud by an 8- μ m radiance standard deviation threshold of 0.5. Clear is then further

defined by 8-minus-11- μ m brightness temperature differences less than 0.5 K and 11-minus-12- μ m differences less than 2.4 K with a further requirement of 11- μ m brightness temperature greater than 277 K. Again, the thresholds were formed after examining differing cloud scenes over a warm water background. If the clear requirements are not met, the decision tree uses 11- μ m brightness temperatures to discern thick water from thick ice cloud. As was previously mentioned, the ice-water cloud division line in the brightness temperature difference scatter diagram will lie near the unity slope. Because mixed-layer, mixed-phase cloud exhibits characteristics of both ice and water clouds, the scatter points tend to fall near this slope. Therefore, once the 8- μ m radiance standard deviation has been established as being greater than 0.5, points falling within 0.3 K of this line, and greater than an 8-minus-11- μ m brightness temperature difference of 1.25 K, are coded as being mixed-phase cloud. This was decided upon by viewing the scatter around the unity slope of Fig. 12. Lastly, pixels not meeting the mixed-cloud-scene requirements are identified as being thin ice cloud if the difference between the 8-minus-11- μ m versus the 11-minus-12- μ m brightness temperature difference is greater than 0.3 K (above the unity slope on the scatter diagram), or nonopaque water cloud if the difference is less than 0.3 K (below the unity slope).

Initial results using this simple technique are encouraging. The coded graphic (Fig. 15c) captures the general features of the image (Fig. 15b) with ice cloud (codes 4 and 2) dominating the upper-right portion, and water cloud and clear (codes 1, 5, and 0) across the bottom quarter. The transition zone is fairly well identified by the mixed-phase code 3 placed around the edges of the main cirrus shield, extending along the left upper edge of the image. The pixels coded 0 follow the general pattern of the warmest brightness temperatures apparent from the image in the lower right-hand corner; however, they appear to underestimate the number of cloud-free pixels. Likewise, areas that appear to be clear from Fig. 15c, are generally coded 1 or 5 across the remainder of the lower portion of the image. This is due to the simplicity of the algorithm, which based the clear-cloudy threshold on data from the 5 December 1991 flight over the Gulf, and applied it to a dataset from a different day, over a different portion of the Gulf. It was shown in section 2 that the amount of water vapor in the atmosphere along with surface radiative features will result in varying clear-cloudy thresholds. A more rigorous technique, one that uses a clustering technique, for instance, will be able to delineate the clear region more accurately for each independent day, without relying on one threshold. Furthermore, since no digital lidar data is available as yet from this flight, it is somewhat difficult from the images alone to tell if a 10 \times 10 pixel is clear. For instance, the darker (warmer) FOVs over the lower left portion of the image are cooler than the warmest

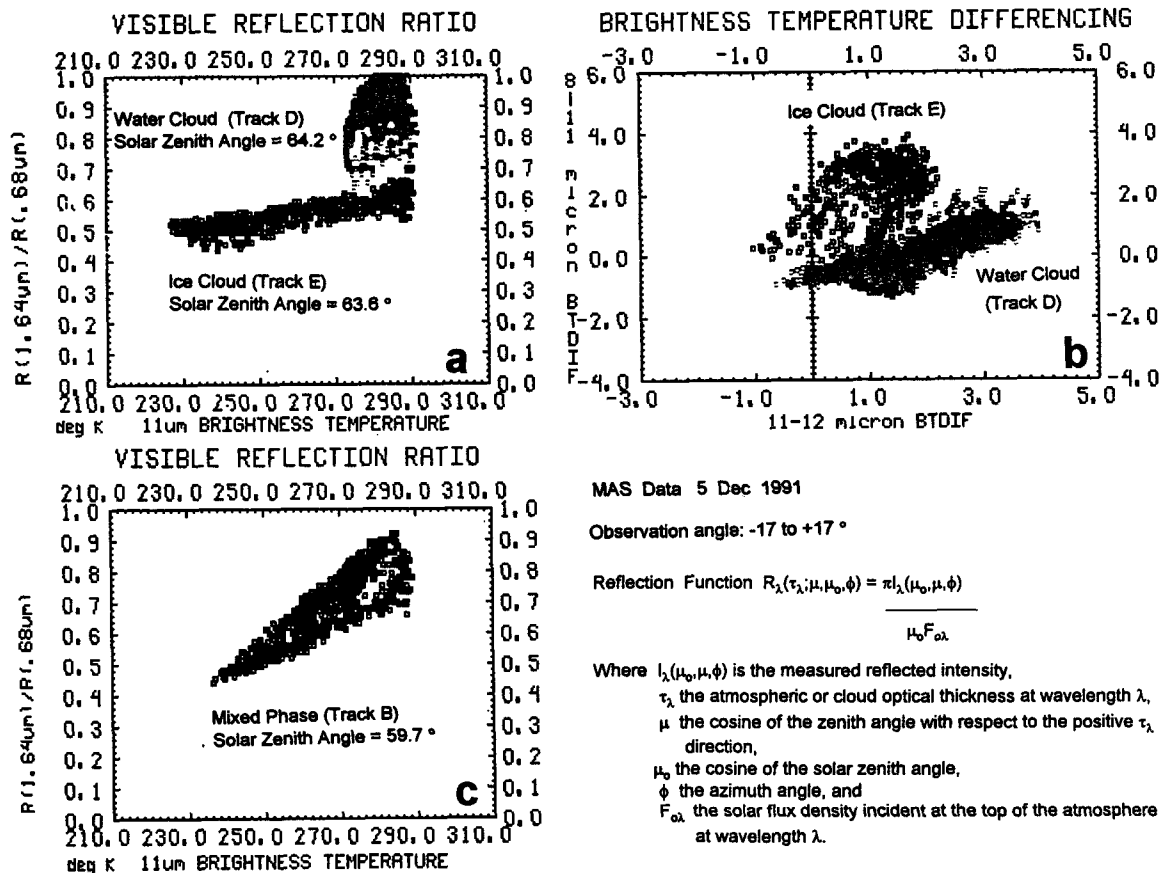


FIG. 16. MAS scatter diagrams from 5 December 1991 of (a) the visible reflection function ratio of a water (track D) and ice (track E) scene, (b) the tripectral brightness temperature differences of the same ice and water scene, and (c) the visible reflection function ratio of a mixed-phase cloud scene (track B).

FOVs in the lower-right corner, and also have areas of even brighter (cooler) patches mixed in next to the patchy clouds in the lower left (Fig. 15a). This hints that the pixels may not be completely cloud free.

From Fig. 12, it is obvious that for low-opacity cirrus and water cloud, some misidentification will occur due to overlap of points near the unity slope (mixed versus pure ice cloud) and just above the clear scatter of points, where the ice cloud and water cloud slopes meet. Further separation of these thin clouds may be possible using cloud microphysical models, or combined with other cloud detection techniques (see section 4).

In summary, the tripectral technique developed in previous sections was tested upon aircraft instrument data from the MAS. Results indicate that the method is able to discern cloud properties; however, a more involved technique will be able to improve the performance, especially in determining clear FOVs.

4. Compatibility with a visible technique

The MODIS instrument will include spectral channels from the visible to the longwave infrared region.

To take full advantage of this broad spectral coverage, it is appropriate to include a comparison of the tripectral method with other proposed MODIS cloud parameterization techniques. An analysis of the strengths and weaknesses of each method when applied to different cloud scenes will aid in the effectiveness of the cloud detection portion of the EOS program.

King et al. (1992) outline a visible reflection function technique for determining cloud phase, which, like the tripectral infrared technique, takes advantage of the difference in the bulk properties of ice versus liquid water. These differences permit phase discrimination by using the ratio of two visible channel reflection functions where one spectral interval has similar absorption coefficients for ice and water (i.e., 0.70 μm), and the other where the values are vastly different (i.e., 1.6 μm , with that of ice being greater than that of water). If the reflection ratio is large, it is indicative of water; conversely, low values indicate ice clouds. For a more complete discussion of the reflection function, see King (1987) and Pilewskie and Twomey (1987).

The MAS FIRE configuration included visible bands centered on 0.68 and 1.64 μm , enabling direct com-

parison of the visible–near-infrared reflection function and infrared trispectral techniques. The visible and near-infrared data were averaged over a $10\text{-pixel} \times 10\text{-pixel}$ box, again yielding 1380 data points spanning a scan angle of $\pm 17^\circ$ from nadir. The reflection ratio was applied to several cloud scenes described in section 3c. Figure 16a is a scatter diagram of the reflectance function ratio versus the $11\text{-}\mu\text{m}$ brightness temperature for MAS 5 December 1991 tracks D (water cloud scene) and E (convective ice cloud scene). A distinct separation is apparent between the ice and water cloud, with an ice–water division threshold of approximately 0.65. For comparison, the trispectral brightness temperature difference scatter diagram for tracks D and E is included (Fig. 16b). Although most of the data points in each track set can be discerned by their coherent patterns, there is overlap between ice and water cloud scenes that cannot be easily separated ($8\text{-minus-}11\text{-}\mu\text{m}$ brightness temperature differences of -1 to 0 K and $11\text{-minus-}12\text{-}\mu\text{m}$ differences between 0.60 and 1.7 K). In this simple single layer, single-phase cloud scene comparison, the visible technique separates ice and water cloud more completely.

Next, the visible ratio technique was applied to the multiphase cloud scene of track B (Fig. 12). The resultant scatter diagram (Fig. 16c) has no easily discernable features. Slopes of water and ice clouds are not consistent with those of Fig. 16a, and there is no hint of the division line between ice and water cloud. The signature cloud patterns evident in the brightness temperature differencing scatter diagram of track B have been extensively documented in section 3c. In this case, more information on cloud parameters can be gained from the trispectral method.

This limited example set indicates the potential usefulness of combining these two techniques. The overlap region of single-layer, single-phase clouds can be more accurately separated with the addition of the visible ratio technique. Multiphase cloud scenes are more easily distinguished with the infrared trispectral method, although neither one displays a clear-cut division between mixed-phase and pure ice clouds and water clouds. However, we note again that infrared techniques have the advantage over visible spectrum methods, because they are not limited to use in daylight hours.

5. Conclusions

Future satellite instruments, including the MODIS, will be expected to reliably and accurately identify cloud, in support of the EOS program. The 8- , 11- , and $12\text{-}\mu\text{m}$ spectral regions are recommended as useful in detecting cloud based on simulations and observations that can be summarized as follows.

- Large positive brightness temperature differences of $8\text{-minus-}11\text{-}\mu\text{m}$ data are indicative of cloud (probably cirrus) while near-zero or negative differences will

indicate clear regions. This is true because particle absorption is a minimum and water vapor absorption is a relative maximum between 8 and $9\text{ }\mu\text{m}$ while conversely, particle absorption peaks and water vapor absorption is relatively weak between 11 and $12\text{ }\mu\text{m}$. The exact clear–cloud threshold value will depend upon the amount of water vapor in the atmosphere and the proximity of the 8- and $11\text{-}\mu\text{m}$ bands to water vapor lines.

- Cloud phase can be determined by plotting $8\text{-minus-}11\text{-}\mu\text{m}$ versus $11\text{-minus-}12\text{-}\mu\text{m}$ brightness temperature differences. Water and ice cloud tend to separate in this format due to different single-scattering properties. Ice and water single-scattering properties differ most near $12\text{ }\mu\text{m}$. This results in a steeper variance of the absorption coefficient from 11 to $12\text{ }\mu\text{m}$ for water than 8 to $11\text{ }\mu\text{m}$, with the reverse holding true for ice cloud.

- Large cloud particle microphysical changes between 10 and $10.8\text{ }\mu\text{m}$ make simulations and detection difficult in this spectral region. This implies that the AVHRR $11\text{-}\mu\text{m}$ bandwidth ($10.3\text{--}11.3\text{ }\mu\text{m}$) is not optimum for use in the trispectral technique.

- The 11- and $12\text{-}\mu\text{m}$ bands should be chosen to maximize the difference in the absorption coefficient, leading to maximum ice–water differentiation. Optimum bands would be near $11\text{ }\mu\text{m}$ and the peak ice absorption of $12\text{ }\mu\text{m}$ (Fig. 1). The VAS [VISSR (Visible–Infrared Spin Scan Radiometer) Atmospheric Sounder] instrument does not take full advantage of the differences, instead overshooting the peak with a central wavelength at $12.66\text{ }\mu\text{m}$.

- Based on a case study using high spatial and spectral resolution HIS data, delineation of high cloud, clear sky, and cloud phase is apparent with the trispectral method. The technique is not degraded using broad $8\text{-}\mu\text{m}$ bandwidths up to $0.8\text{ }\mu\text{m}$. The technique is also effective across a large section of the $8\text{-}\mu\text{m}$ spectral region. This means that the $8\text{-}\mu\text{m}$ bandwidth selection is adjustable for cloud detection, and therefore can be selected based on other applications.

- The trispectral method applied to operational polar orbiting data has difficulty delineating cloud phase; large footprint sizes detect too many nonuniform cloud scenes, which leads to blurring of the distinct cloud parameter thresholds seen in the 2-km and finer-scale data. Screening out nonuniform cloud scenes results in a dataset to which the technique can be applied.

- The cloud-detection technique was used on a high spatial resolution MAS dataset over a variety of cloud scenes, from which an algorithm for identifying cloud properties was developed. Results were encouraging even when using a very simple thresholding technique. Cloud phase and effective emissivity consistent with the image was discerned along with clear regions. A more rigorous algorithm would allow the method to be applied to varying atmospheric and surface scenes.

- The sensitivity of the trispectral technique to brightness temperature difference (less than 1 K) requires very good channel-to-channel registration. No current satellite instrument includes all three bandwidths.

- Combination of infrared trispectral and visible reflectance ratio methods will yield the most complete cloud depiction.

The opportunities for global cloud delineation with MODIS appear excellent. The trispectral technique seems appropriate and will be complemented by CO₂ slicing (Menzel et al. 1992) to characterize cloud height and amount. The spectral selection, the spatial resolution, and the global coverage are all well suited for significant advances.

Acknowledgments. The authors would like to acknowledge the contributions of Chris Moeller at SSEC/CIMSS and the ER2 and MODIS Airborne Simulator field teams. This work was supported by the National Aeronautics and Space Administration under Contracts NAS5-31367 and NAG1-1177.

REFERENCES

- Ackerman, S. A., W. L. Smith, J. D. Spinhirne, and H. E. Revercomb, 1990: The 27–28 October 1986 FIRE IFO cirrus case study: Spectral properties of cirrus clouds in the 8–12 μm window. *Mon. Wea. Rev.*, **118**, 2377–2388.
- , R. A. Frey, and W. L. Smith, 1992: Radiation budget studies using collocated observations from AVHRR, HIRS/2, and ERBE instruments. *J. Geophys. Res.*, **97**, 11 513–11 525.
- Aoki, T., 1980: A method for matching the HIRS-2 and AVHRR pictures of *TIROS-N* satellites. Meteorological Satellite Center Tech. Note 2, Tokyo, Japan, 15–26.
- Booth, A. L., 1973: Objective cloud type classification using visual and infrared satellite data. *Preprints, Third Conf. on Probability and Statistics in the Atmospheric Sciences*. Boulder, CO, Amer. Meteor. Soc., 220–227.
- Inoue, T., 1987: A cloud type classification with NOAA 7 split window measurements. *J. Geophys. Res.*, **92**, 3991–4000.
- , 1989: Features of clouds over the tropical Pacific during the Northern Hemispheric winter derived from split window measurements. *J. Meteor. Soc. Japan*, **67**, 621–637.
- King, M. D., 1987: Determination of the scaled optical thickness of clouds from reflected solar radiation measurements. *J. Atmos. Sci.*, **44**, 1734–1751.
- , Y. J. Kaufman, W. P. Menzel, and D. Tanre, 1992: Remote sensing of cloud, aerosol, and water vapor properties from the Moderate Resolution Imaging Spectrometer (MODIS). *IEEE Trans. Geosci. Remote Sens.*, **30**, 2–27.
- Menzel, W. P., D. P. Wylie, and K. I. Strabala, 1992: Seasonal and diurnal changes in cirrus clouds as seen in four years of observations with the VAS. *J. Appl. Meteor.*, **31**, 370–385.
- Pilewskie, P., and S. Twomey, 1987: Discrimination of ice from water in clouds by optical remote sensing. *Atmos. Res.*, **21**, 113–122.
- Smith, W. L., H. E. Revercomb, H. B. Howell, H. M. Woolf, and D. D. LaPorte, 1986: The High Resolution Interferometer Sounder (HIS). CIMMS View, Vol II, No. 3, University of Wisconsin, 1–5.
- , H. M. Woolf, and H. E. Revercomb, 1991: Linear simultaneous solution of temperature and absorbing constituent profiles from radiance spectra. *Appl. Optics*, **30**, 1117–1123.
- Takano, Y., K. N. Liou, and P. Minnis, 1992: The effects of small ice crystals on cirrus infrared radiative properties. *J. Atmos. Sci.*, **49**, 1487–1493.
- Warren, S. G., 1984: Optical constants of ice from the ultraviolet to the microwave. *Appl. Optics*, **23**, 1206–1225.